



HAL
open science

Extension of the cone-beam CT field-of-view using two complementary short scans

Gabriele Belotti, Giovanni Fattori, Guido Baroni, Simon Rit

► **To cite this version:**

Gabriele Belotti, Giovanni Fattori, Guido Baroni, Simon Rit. Extension of the cone-beam CT field-of-view using two complementary short scans. *Medical Physics*, 2024, 51 (5), pp.3391-3404. 10.1002/mp.16869 . hal-04320045v2

HAL Id: hal-04320045

<https://hal.science/hal-04320045v2>

Submitted on 12 May 2024

HAL is a multi-disciplinary open access archive for the deposit and dissemination of scientific research documents, whether they are published or not. The documents may come from teaching and research institutions in France or abroad, or from public or private research centers.

L'archive ouverte pluridisciplinaire **HAL**, est destinée au dépôt et à la diffusion de documents scientifiques de niveau recherche, publiés ou non, émanant des établissements d'enseignement et de recherche français ou étrangers, des laboratoires publics ou privés.



Distributed under a Creative Commons Attribution - NonCommercial 4.0 International License

Extension of the cone-beam CT field-of-view using two complementary short scans

Gabriele Belotti¹ | Giovanni Fattori² | Guido Baroni^{1,3} | Simon Rit⁴

¹Department of Electronics, Information and Bioengineering, CartCasLab, Politecnico di Milano (MI), Milan, Italy

²Center for Proton Therapy, Paul Scherrer Institute, Villigen, Switzerland

³Centro Nazionale di Adroterapia Oncologica (CNAO), Pavia (PV), Italy

⁴Univ Lyon, CREATIS, INSA-Lyon, Université Claude Bernard Lyon 1, UJM-Saint Etienne, CNRS, Inserm, CREATIS UMR5220, U1294, Lyon, France

Correspondence

Gabriele Belotti, Department of Electronics, Information and Bioengineering, CartCasLab, Politecnico di Milano (MI), Milan, Italy.
Email: gabriele.belotti@polimi.it

Funding information

CNAO Foundation, Grant/Award Number: BAA9CONV01; SIRIC LYriCAN+, Grant/Award Number: INCa-DGOS-INSERM-ITMO cancer_18003; LABEX PRIMES, Grant/Award Numbers: ANR-11-LABX-0063, ANR-11-IDEX-0007

Abstract

Background: Robotic C-arm cone-beam computed tomography (CBCT) scanners provide fast in-room imaging in radiotherapy. Their mobility extends beyond performing a gantry rotation, but they might encounter obstructions to their motion which limit the gantry angle range. The axial field-of-view (FOV) of a reconstructed CBCT image depends on the acquisition geometry. When imaging a large anatomical location, such as the thorax, abdomen, or pelvis, a centered cone beam might be insufficient to acquire untruncated projection images. Some CBCT scanners can laterally displace their detector and collimate the beam to increase the FOV, but the gantry must then perform a 360° rotation to provide complete data for reconstruction.

Purpose: To extend the FOV of a CBCT image with a single short scan (gantry angle range of 180° + fan angle) using two complementary short scans.

Methods: We defined an acquisition protocol using two short scans during which the source follows the same trajectory and where the detector has equal and opposite tilt and/or offset between the two scans, which we refer to as complementary scans. We created virtual acquisitions using a Monte Carlo simulator on a digital anthropomorphic phantom and on a computed tomography (CT) scan of a patient abdomen. For our proposed method, each simulation produced two complementary sets of projections, which were weighted for redundancies and used to reconstruct one CBCT image. We compared the resulting images to the ground truth phantoms and simulations of conventional scans.

Results: Reconstruction artifacts were slightly more prominent in the complementary scans w.r.t. a complete scan with untruncated projections but matched those in a single short scan without truncation. When analyzing reconstructed scans from simulated projections with scatter and corrected with prior CT information, we found a global agreement between complementary and conventional scan approaches.

Conclusions: When dealing with a limited range of motion of the gantry of a CBCT scanner, two complementary short scans are a technically valid alternative to a full 360° scan with equal FOV. This approach enables FOV extension without collisions or hardware upgrades.

KEYWORDS

CBCT, double short-scans, field-of-view

This is an open access article under the terms of the [Creative Commons Attribution-NonCommercial](https://creativecommons.org/licenses/by-nc/4.0/) License, which permits use, distribution and reproduction in any medium, provided the original work is properly cited and is not used for commercial purposes.

© 2023 The Authors. *Medical Physics* published by Wiley Periodicals LLC on behalf of American Association of Physicists in Medicine.

1 | INTRODUCTION

Cone-beam computed tomography (CBCT) is a common three-dimensional radiographic imaging option for image-guided radiotherapy (IGRT). Integrated as an on-board treatment unit imager or as a stand-alone in-room solution, CBCT provides soft tissue imaging for daily treatment verification without the burden of a diagnostic computer tomography (CT) scanner. Often configured as an isocentric imaging system, the simplicity and small footprint of the hardware have enabled a variety of CBCT solutions,¹ including remote C-arm imaging,² couch-mounted³ and nozzle-mounted⁴ alternatives.

In such compact systems, a common concern is the field of view (FOV) size in the axial plane for imaging wide patient's sites, for example, thorax, abdomen, or pelvis. Given appropriate hardware – namely: adjustable collimator, wide cone angle x-ray tube, and movable flat panel detector – the CBCT FOV can be extended with a full circular scan (i.e., 360° source rotation) by laterally displacing the detector from the conventional position where the source-to-center line hits the detector at its center.^{5,6} Such displaced detector (DD) acquisition is often referred to as half fan (Figure 1, right panel) in contrast to the conventional centered detector one, called full fan (FF).

Previous works suggested that multiple scans could also be combined to virtually increase the system's lateral angle⁷ or achieve sufficient data for short (less than 360°) scan⁸ reconstruction.⁹ A case study of FOV extension in a limited range of motion¹⁰ is the robotic CBCT scanner currently in use at the CNAO (Figure 2). This scanner offers a displaced center of rotation (DCoR) geometry¹¹ by decoupling the robotic

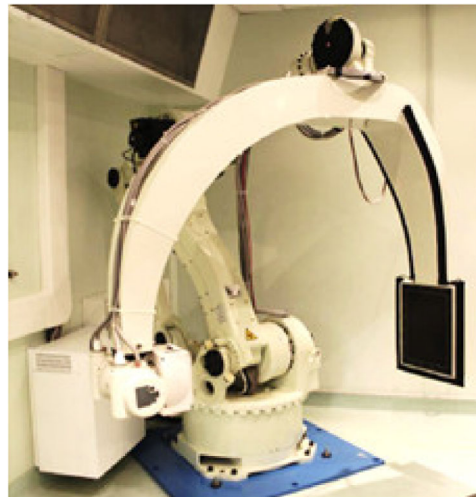


FIGURE 2 Robotic CBCT scanner inside CNAO central room. The sixth joint mounts the custom C-arm, which supports the x-ray tube plus fixed collimator assembly, aligned to the detector. CBCT, cone-beam computed tomography.

end-effector (tooltip T) from the imaging isocenter I. The acquisition geometry is depicted on the left-hand side of Figure 1 and can be used to acquire two complementary short scans as illustrated in the left panel of Figure 3. The x-ray source visits the same short scan arc of trajectory twice with opposite detector tilt angles (τ_1 and τ_2), that is, the angle between the flat panel orthogonal and the source to center of rotation line. The approach was named complementary displaced centers of rotation (C-DCoR) acquisition due to the complementarity of projection data from both rotations necessary for the reconstruction. A CBCT image with sufficient FOV provides complete anatomical information to the

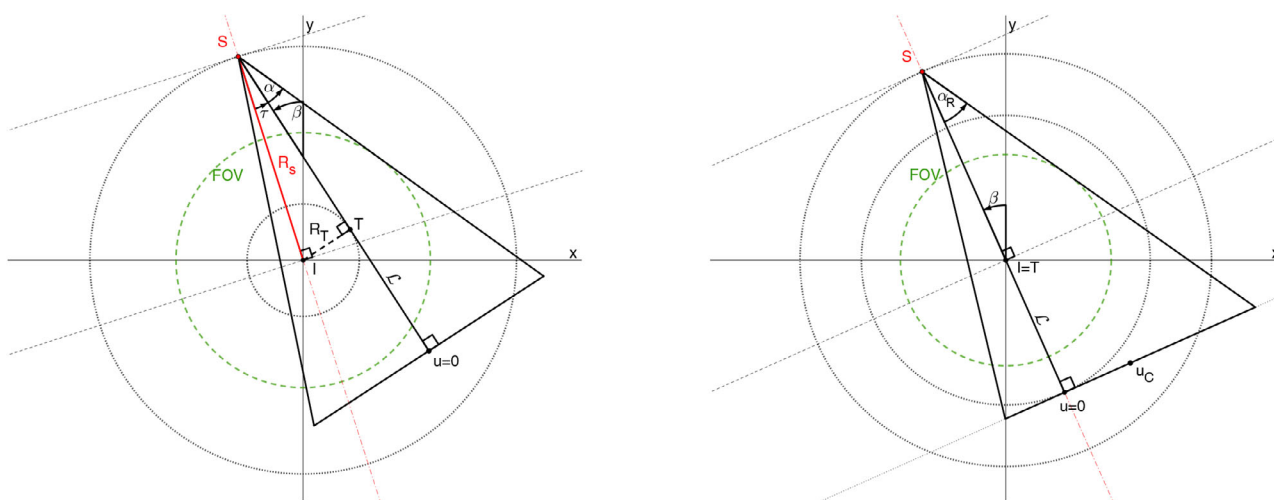


FIGURE 1 The two proposed acquisition geometries to enlarge the FOV. Left: DCoR geometry in plane $z = 0$. The detector and source S are bound together as in the conventional FF geometry while S travels the circle with radius R_s . The detector is tilted by an angle τ and the tooltip T travels at a constant distance R_T from I. Right: DD circular geometry in plane $z = 0$. Both the source and the detector revolve around I, the first at a radius equal to the STD and the second on a radius equal to $SDD - STD$ (where SDD is the source-detector distance). The detector is untilted (i.e. orthogonal to the source-to-isocenter line) so that $R_T = 0$ and $I = T$ but has been offset in the positive u direction. DCoR, displaced center of rotation; DD, displaced detector; FF, full fan; FOV, field-of-view; STD, source-to-tooltip distances.

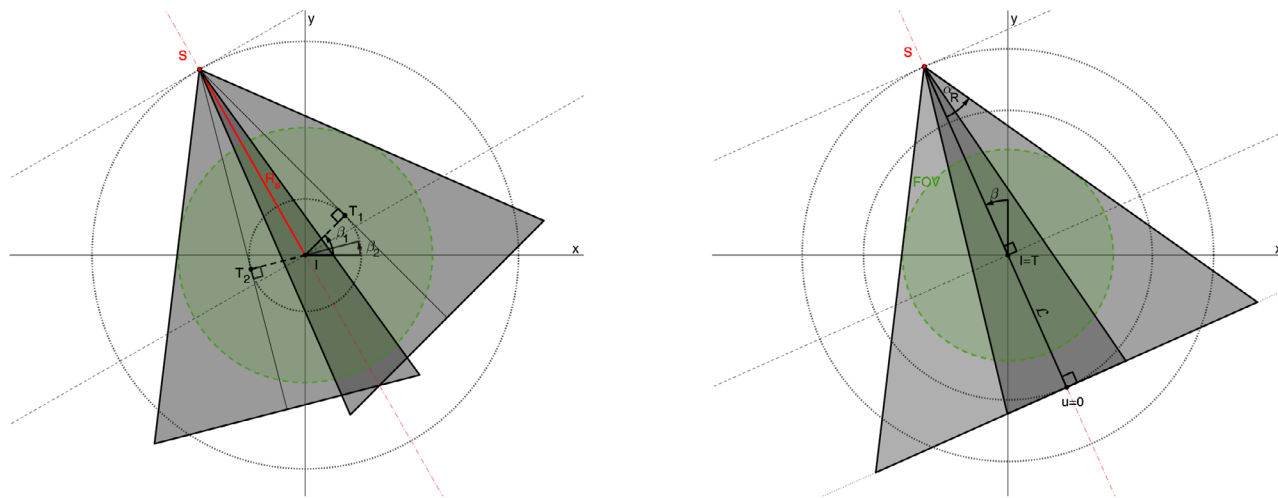


FIGURE 3 Left: C-DCoR scans with $\tau_1 = -\tau_2$ and $\beta_2 = \beta_1 - 2\tau_1$ such that the source is at the same position $S(\tau_1, \beta_1, 0) = S(\tau_2, \beta_2, 0)$ in the two arcs. Right: C-DD scans with gantry angle $\beta_2 = \beta_1$ since the source follows $S(0, \beta_1, 0) = S(0, \beta_2, 0)$ in the two arcs. No tilt is applied but there is a detector offset $u_{C1} = -u_{C2}$. C-DCoR, complementary displaced centers of rotation; C-DD, complementary displaced detector.

clinician moments before treatment delivery, used for patient position verification and adaptive radiotherapy.¹² Any scanner with a limited range of motion, regardless of tilting or detector offset capability, could benefit from a FOV extension strategy using complementary scans. Recently, some authors presented a similar strategy tailored to the Imaging Ring system,¹³ further highlighting the interest in this type of acquisition protocols. The current work exploits a couple of short scans⁸ to obtain the same FOV as a complete 360° DCoR or DD scan would produce. Our aim is to derive and evaluate a filtered-backprojection reconstruction algorithm for this geometry and Complementary Displaced Detector (C-DD) strategies, that is, when the detector is not tilted but offset laterally (Figures 1 and 3, right panels). Cone beam imaging is particularly prone to artifacts due to scatter radiation, significantly reducing image quality, whose extent and severity are a function of the acquisition geometry. Therefore, full scans and complementary short scans acquisitions were simulated using Monte Carlo to study the effect of scatter and beam hardening in the proposed methods using a computational Forbild thorax phantom and a patient CT image of an abdomen. Image quality was evaluated after applying state-of-the-art scatter and beam hardening correction methods.

2 | MATERIALS AND METHODS

2.1 | Circular trajectory scan

The geometry of the CBCT scanner is presented in Figure 1 in the central plane $z = 0$ of the trajectory of the source S. The source rotates around the isocenter

I , which is the center of the coordinate system. We note β the gantry angle between the y -axis and the source-to-detector line (\mathcal{L}), perpendicular to the detector. The transaxial detector coordinate is u such that $u = 0$ where \mathcal{L} intersects the detector. The position of the detector can be adjusted in the u direction but is fixed during a scan arc. We note u_C the coordinate of the detector center. In addition, we define the detector tilt angle τ between the source-to-isocenter line and \mathcal{L} . The two angles β and τ are positive in the counter-clockwise direction. For every analyzed strategy, the source point follows a circular trajectory, centered on I with a radius R_S , such that the source is at $S(\tau, \beta) = R_S \mathbf{e}_S$ with the unit vector $\mathbf{e}_S = (-\sin(\beta - \tau), \cos(\beta - \tau), 0)$. Since the setup is a robotic CBCT, we define the tooltip point T as a construction-defined point w.r.t. the C-arm corresponding to the robotic end-effector. The source-to-detector (SDD) and the source-to-tooltip (STD) are fixed by the C-arm design. The tooltip also follows a circle of center I and radius $R_T = \sqrt{R_S^2 - \text{STD}^2}$ such that $T(\beta) = R_T(\cos \beta, \sin \beta, 0)$.

We define three geometries:

1. FF geometry: when $\tau = 0$, $R_S = \text{STD}$ and $u_C = 0$, which is the conventional circular cone-beam geometry (not shown in Figure 1).
2. DCoR geometry: when $\tau \neq 0$, $R_S = \sqrt{\text{STD}^2 + R_T^2}$ and $u_C = 0$ (Figure 1 left).
3. DD geometry: when $\tau = 0$, $R_S = \text{STD}$ and $u_C \neq 0$ (Figure 1 right).

We note $\alpha = \arctan(N_u \Delta_u / (2 \text{SDD}))$ the angle between the SDD line \mathcal{L} and the ray at the detector edge, with N_u the number of pixels of the detector

in the transaxial direction and Δ_u their spacing. We note α_u the angle between the ray impinging on the detector pixel at coordinate $(u, 0)$ and the source-to-isocenter line, given by

$$\alpha_u = \tau + \arctan\left(\frac{u}{\text{SDD}}\right), \quad (1)$$

where $u \in [u_L, u_R]$, $u_L = u_C - N_u \Delta_u / 2$, $u_R = u_C + N_u \Delta_u / 2$, and $\alpha_u \in [\alpha_L, \alpha_R]$ is the associated angle. If α_L and α_R have opposite signs, the source-to-isocenter line hits the detector and the proposed strategies could achieve exact reconstruction in the central slice of the FOV with radius $R_{\text{FOV}} = R_S \sin(\max(|\alpha_L|, |\alpha_R|))$.

2.2 | Reconstruction

Let g be the set of cone-beam projections acquired by one of the FF, DD or DCoR geometries and modeled by the line integral

$$g_\tau(\beta, u, v) = \int f(S(\tau, \beta) + l \mathbf{r}_{\tau, \beta, u, v}) dl, \quad (2)$$

where

$$\mathbf{r}_{\tau, \beta, u, v} = \frac{(R_T + u) \mathbf{e}_u + v \mathbf{e}_v + (\text{SDD} - \text{STD}) \mathbf{e}_w}{\|(R_T + u) \mathbf{e}_u + v \mathbf{e}_v + (\text{SDD} - \text{STD}) \mathbf{e}_w\|} \quad (3)$$

is the unit vector pointing from the source S to the (u, v) position on the detector. The unit vectors $\mathbf{e}_u = (\cos \beta, \sin \beta, 0)$, $\mathbf{e}_v = (0, 0, 1)$, and $\mathbf{e}_w = (\sin \beta, -\cos \beta, 0)$ define a coordinate system oriented by the detector. Recalling that Tuy's condition for exact reconstruction¹⁴ is respected only in the source plane $z = 0$, we employ the approximate 3D reconstruction formula of Rit et al.¹⁵ based on FDK's algorithm¹⁶ to find the unknown target density $f(\mathbf{x})$

$$f(\mathbf{x}) \simeq \mathcal{R}g(\mathbf{x}) = \frac{1}{2} \int_0^{2\pi} \frac{1}{U^2} \int_{\mathbb{R}} \cos \alpha_u \frac{R_S}{\text{SDD}} g_\tau(\beta, u, v^*) \times h(u^* - u) du dv \quad (4)$$

with the magnification factor

$$U = \frac{\text{STD} + \mathbf{x} \cdot \mathbf{e}_w}{\text{SDD}} \quad (5)$$

and the ramp filter

$$h(u) = \int |k_u| \exp(2\pi i u) k_u dk_u. \quad (6)$$

2.2.1 | Short scan weights

A common practice in the FF case is to acquire a short scan of $\pi + 2\alpha_R$ and to use Parker pre-reconstruction

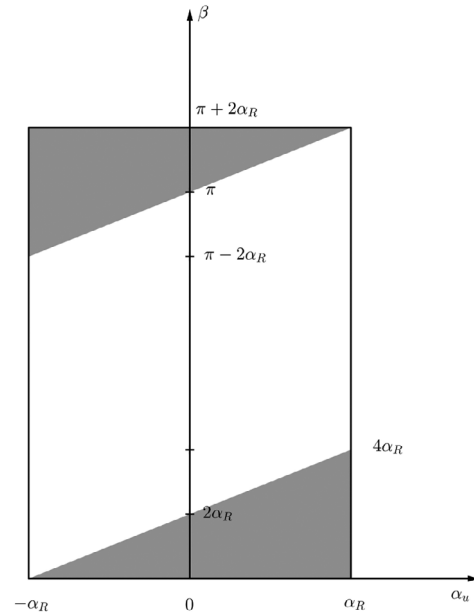


FIGURE 4 Short scan weights map describing two redundancy zones of the projections. The shaded parts are measured twice while the central part is measured once. A smoothing function for the shaded areas is adapted from Parker's one.⁸

weights⁸

$$w_P(\beta, u, v) = \begin{cases} \sin^2\left(\frac{\pi}{4} \frac{\beta}{\alpha_R - \alpha_u}\right) & \text{if } 0 \leq \beta \leq 2\alpha_R - 2\alpha_u, \\ \sin^2\left(\frac{\pi}{4} \frac{\pi + 2\alpha_R - \beta}{\alpha_R + \alpha_u}\right) & \text{if } \pi - 2\alpha_u \leq \beta \leq \pi + 2\alpha_R, \\ 1 & \text{otherwise.} \end{cases} \quad (7)$$

Weights and notation were adapted to our geometry, and a representation of a short scan redundancy map is provided in Figure 4. We apply Equation (4) $f \simeq \mathcal{R}\{w_P g\}$ (with the range of the first integral set to $\beta \in [0, \pi + 2\alpha_R]$).

2.2.2 | DD weights

When dealing with any DD, regardless of the scan range, we followed the approach of refs. [5, 6] to handle the redundancies caused by the detector offset. We multiply the projections with weights

$$w_D(\beta, u, v) = \begin{cases} \frac{1}{2} \left(\text{sign}(\alpha_L + \alpha_R) \sin\left(\frac{\pi \alpha_u}{2\theta}\right) + 1 \right) & \text{if } |\alpha_u| < \theta, \\ 1 & \text{otherwise,} \end{cases} \quad (8)$$

where $\theta = \min(-\alpha_L, \alpha_R)$ coincides with the limit of the redundant part of the detector, as shown in Figure 5. To reconstruct complete scans with DD, we use $f \simeq \mathcal{R}\{w_D g\}$.

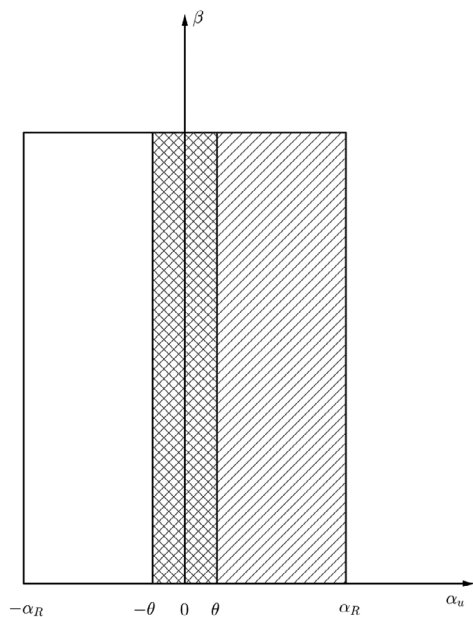


FIGURE 5 Displaced detector weights map describing two redundancy zones of the projections. The internal part is measured twice, while the external one is measured once. We show here the case of a positive displacement where $\alpha_R > |\alpha_L|$ and $\theta = -\alpha_L$.

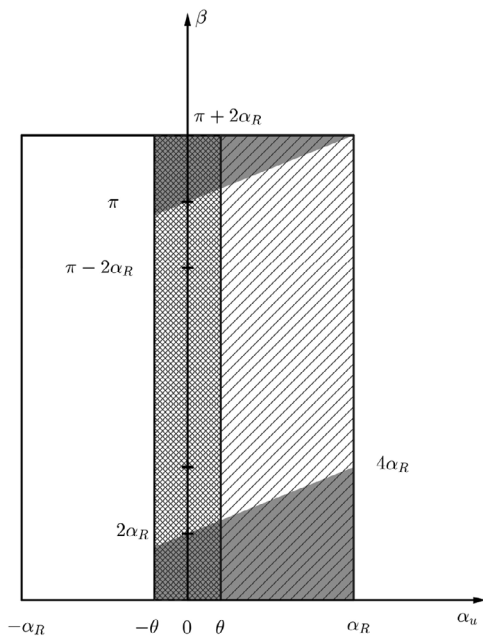


FIGURE 6 Redundancy weights map resulting from the multiplication of the short scan and displaced detector weights maps, when the offset is positive. The projections part from $-\alpha_R$ to $-\theta$ is measured by the complementary scan and weighted by a similar map obtained by rotating this one by π around the center $(0, \pi/2 + \alpha_R)$.

2.2.3 | Complementary scans

If two complementary short scans with mirrored offsets are acquired, all the ray line integrals of a single FF scan are acquired, and one can reconstruct the same image as a single FF short scan if the redundancies

TABLE 1 Parameters for the simulations.

	FF	FF212°	DD	C-DCoR	C-DD
SDD (mm)	1600	1600	1600	1600	1600
STD (mm)	1102.91	1102.91	1102.91	1100	1102.91
FOV (mm)	403	403	366	363	366
N_u (pix)	1536	1536	768	768	768
N_v (pix)	1024	1024	1024	1024	1024
$\Delta_u = \Delta_v$ (mm/pix)	0.388	0.388	0.388	0.388	0.388
α (°)	10.55	10.55	5.32	5.32	5.32
τ_1 (°)	0	0	0	4.159	0
R_T (mm)	0	0	0	80	0
u_{C1} (mm)	0	0	120	0	120
R_S (mm)	1102.91	1102.91	1102.91	1102.91	1102.91

Note: DD and C-DD have the same SDD but STD = 1102.91 mm to achieve a source trajectory identical to that of DCoR for comparison purposes. Abbreviations: C-DCoR, complementary displaced centers of rotation; C-DD, complementary displaced detector; DD, displaced detector; FF, full fan, FOV, field-of-view; SDD, source-to-detector; STD, source-to-toollip distances.

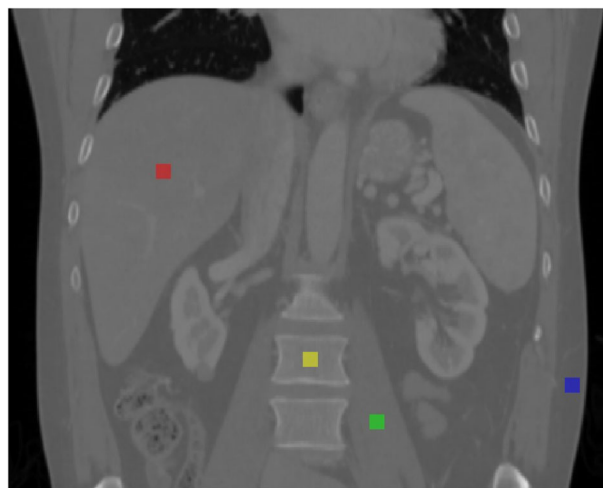


FIGURE 7 ROIs extracted from the CT. Red, blue, green, and yellow are liver, fat, muscle, and bone marrow respectively. CT, computed tomography.

are accounted for by appropriate weights. We then have $\tau_1 = -\tau_2$ to enforce the same source trajectory during the two arcs, that is, $S(\tau_1, \beta) = S(\tau_2, \beta - 2\tau_1)$, as shown in Figure 3. The acquired projection datasets $g_1(\beta, u, v)$ and $g_2(\beta, u, v)$ are weighted and reconstructed separately. Figure 6 depicts the final redundancy map for g_1 . This comes down to reconstructing $f \simeq \mathcal{R}\{w_{P_1} w_{D_1} g_1\} + \mathcal{R}\{w_{P_2} w_{D_2} g_2\}$ where β takes values in two ranges, both spanning $\pi + 2 \max(-\alpha_L, \alpha_R)$ with an offset of $2\tau_1$ in each scan to cover the same source trajectory in each short scan. Note that the two sinograms g_1 and g_2 require both short scan weights from Equation (7) and DD weights from Equation (8).

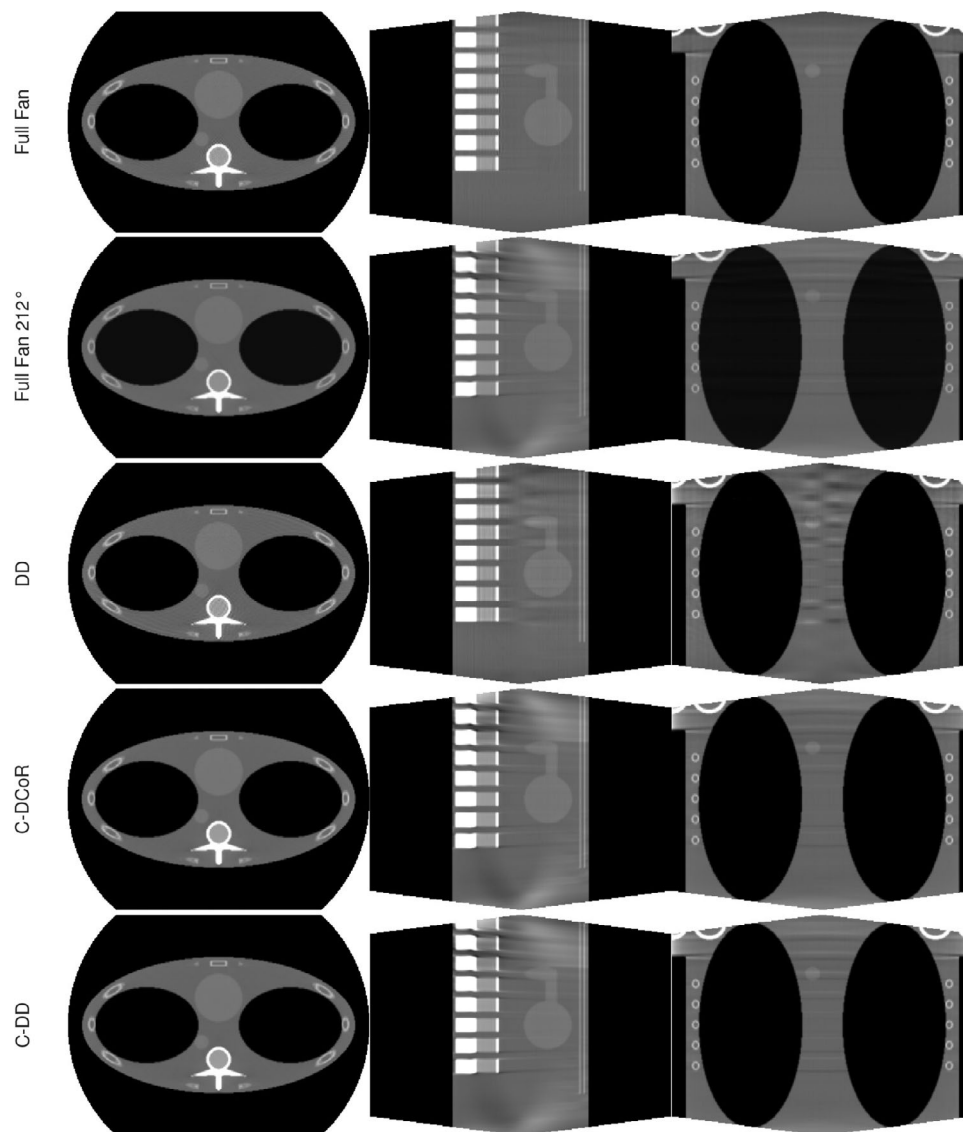


FIGURE 8 Primary-only results for the Forbild thorax phantom. The window/level is 1200/0 HU.

2.3 | Simulations

We produced primary (P_{MC}) and scatter (S_{MC}) x-ray images using MC simulations based on the approach of ref. [17] for several acquisition geometries using a digital Forbild thorax phantom and the CT of a pancreatic patient extracted from The Cancer Imaging Archive.¹⁸ All MC simulations were achieved using GATE v9.2 (based on Geant4 v11).¹⁹ The simulations used fixed forced detection, a variance reduction technique to limit the computation time. The energy-dependent efficiency of the detector was that of the Varian Paxscan 4030D, computed from knowledge of the detector design provided by the manufacturer. The x-ray fluence spectrum was computed by the open-source software SpekPy²⁰ at 90 kVp with 3.2 mm Al filtration. The tube, a Varian A-277, features a 7° rhenium-tungsten molybdenum tar-

get. We ran one MC simulation per phantom for each analyzed acquisition strategy, each one with a detector with isometric pixel spacing $\Delta_u = \Delta_v = 0.388$ mm and size $N_u \times N_v = 768 \times 1024$ pixels, except for FF and FF212° which had a doubled size $N_u = 1536$ pixels to depict a hardware upgrade scenario with a hypothetical detector. All parameters are reported in Table 1.

For FF and DD, each phantom was projected onto 460 discrete projections in a 360° gantry arc. For C-DD and C-DCoR, the two arcs were of 212° for a total of 920 primary projections. Finally, the FF212° acquisition was simulated onto the same short scan arc as the complementary strategies, for a total of 460 projections. To accelerate the photon transport calculation, scatter was simulated at a downsampled resolution (eight times), with an angular spacing $\Delta\beta = 5^\circ$ and a statistical uncertainty < 5%. After the simulation, the scatter images were

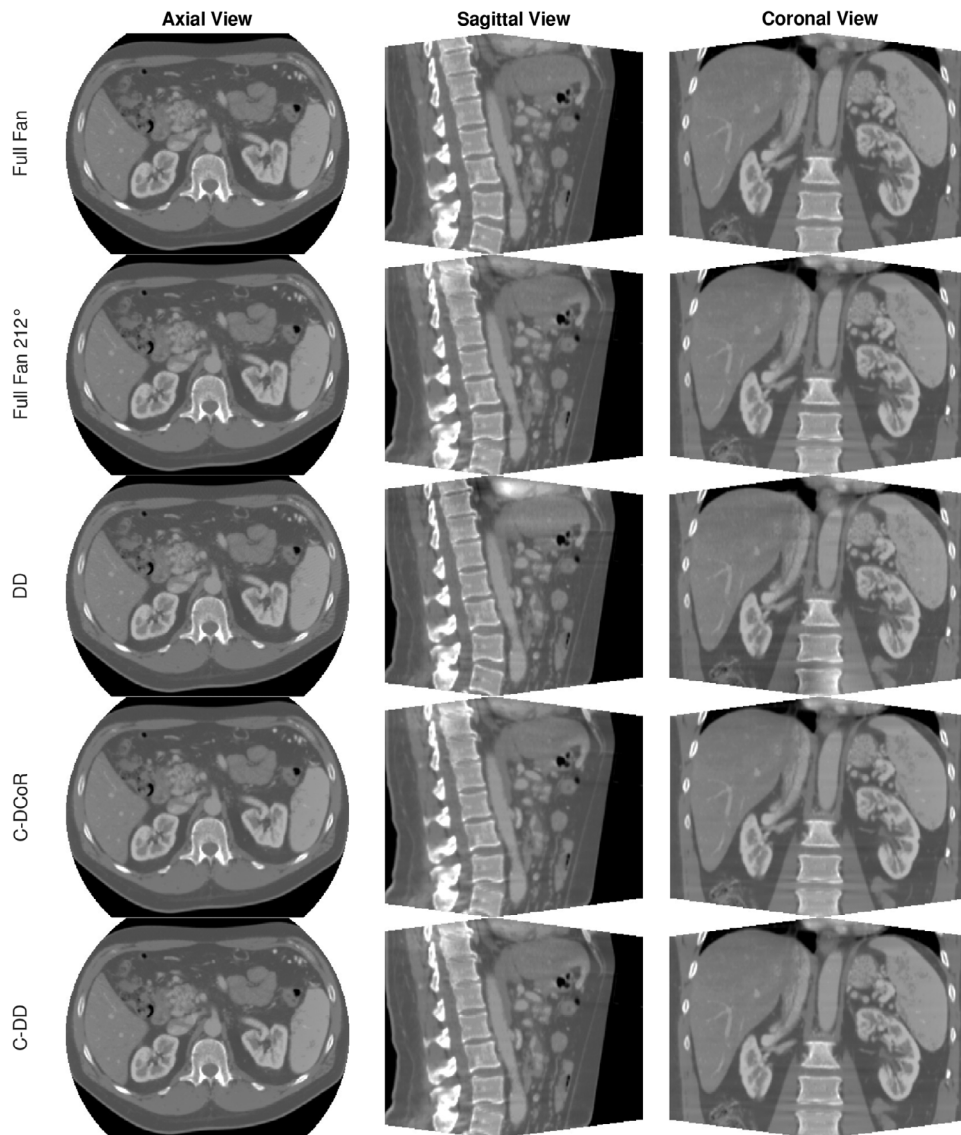


FIGURE 9 Primary-only results for the patient-derived CBCT. The window/level is 1200/0 HU. CBCT, cone-beam computed tomography.

adequately upsampled and their intensity rescaled to match the simulation of primary projections.

2.4 | Pre-processing and reconstruction

Two projection datasets were produced from each simulation. First, primary projections were scaled to attenuation using the following

$$g_P = -\ln\left(\frac{I_P}{I_0}\right), \tag{9}$$

where I_0 represents the flat field image – without attenuating object – generated by our simulation. The projections were corrected for beam hardening using a polynomial approach:

$$\tilde{g}_P = a g_P + b g_P^2 + c g_P^3. \tag{10}$$

TABLE 2 Global MAE and insert ME in primary images w.r.t. ground truth images.

		FF	FF212°	DD	C-DCoR	C-DD
Forbild	MAE (HU)	44	51	46	52	51
	ME - Bone (HU)	-27	-33	-25	-30	-31
Patient	MAE (HU)	23	29	28	31	31
	ME - Bone (HU)	-74	-3	-59	1	17
	ME - Bone marrow (HU)	35	33	34	37	35
	ME - Fat (HU)	-17	-1	28	36	35
	ME - Muscle (HU)	1	32	89	35	35
	ME - Liver (HU)	-8	-8	-7	-4	-4

Note: The error was extracted inside the FOV of the C-DCoR reconstruction, which is the smaller of the set, excluding all air and objects outside the skin perimeter.

Abbreviations: C-DCoR, complementary displaced centers of rotation; C-DD, complementary displaced detector; DD, displaced detector; FF, full fan, FOV, field-of-view; MAE, mean absolute error; ME, mean error.

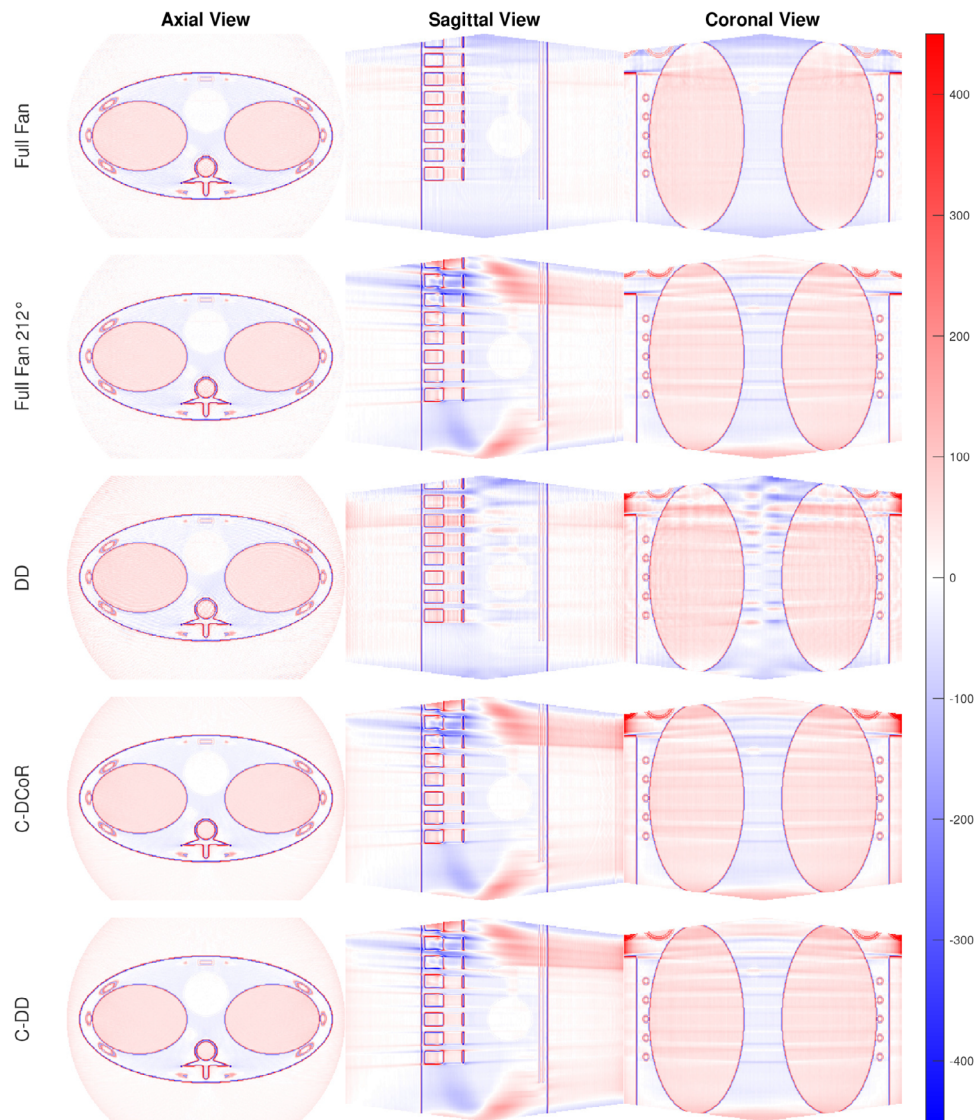


FIGURE 10 Primary-only difference maps for views in Figure 8. The window/level is 900/0 HU. Note the pattern for FF212°, C-DCoR and C-DD sagittals, related to the short scan acquisition. C-DCoR, complementary displaced centers of rotation; C-DD, complementary displaced detector.

We found values of $a, b, c = [42.588, 0.534, -0.011]$ by fitting the average attenuation in water given by our spectrum and the corresponding crossed path lengths from 1 to 1000 mm. We then applied the approach of Joseph and Spital for bone-specific beam hardening correction.²¹ The second projection dataset is made of scatter-corrupted projections obtained by adding the scatter contribution I_S :

$$g_{MC} = -\ln\left(\frac{I_P + I_S}{I_0}\right). \quad (11)$$

For scatter correction, we applied the projection domain scatter correction pipeline based on prior CT information described by several works,^{22–24} following closely the implementation of Zöllner et al. In brief, the method requires the forward projection of the

TABLE 3 Global error of primary plus scatter images w.r.t. ground truth images.

		FF	FF212°	DD	C-DCoR	C-DD
Forbild	MAE (HU)	23	37	28	37	37
	ME - Bone (HU)	-51	-54	-54	-56	-55
Patient	MAE (HU)	14	19	24	29	28
	ME - Bone (HU)	-31	-16	-29	-22	26
	ME - Bone marrow (HU)	3	0	2	7	7
	ME - Fat (HU)	18	21	64	73	71
	ME - Muscle (HU)	6	31	98	39	39
	ME - Liver (HU)	8	3	7	12	12

Note: The error was extracted inside the FOV of the C-DCoR reconstruction, which is the smaller of the set, excluding air outside the skin perimeter. Abbreviations: C-DCoR, complementary displaced centers of rotation; C-DD, complementary displaced detector; DD, displaced detector; FF, full fan, FOV, field-of-view; MAE, mean absolute error, ME, mean error.

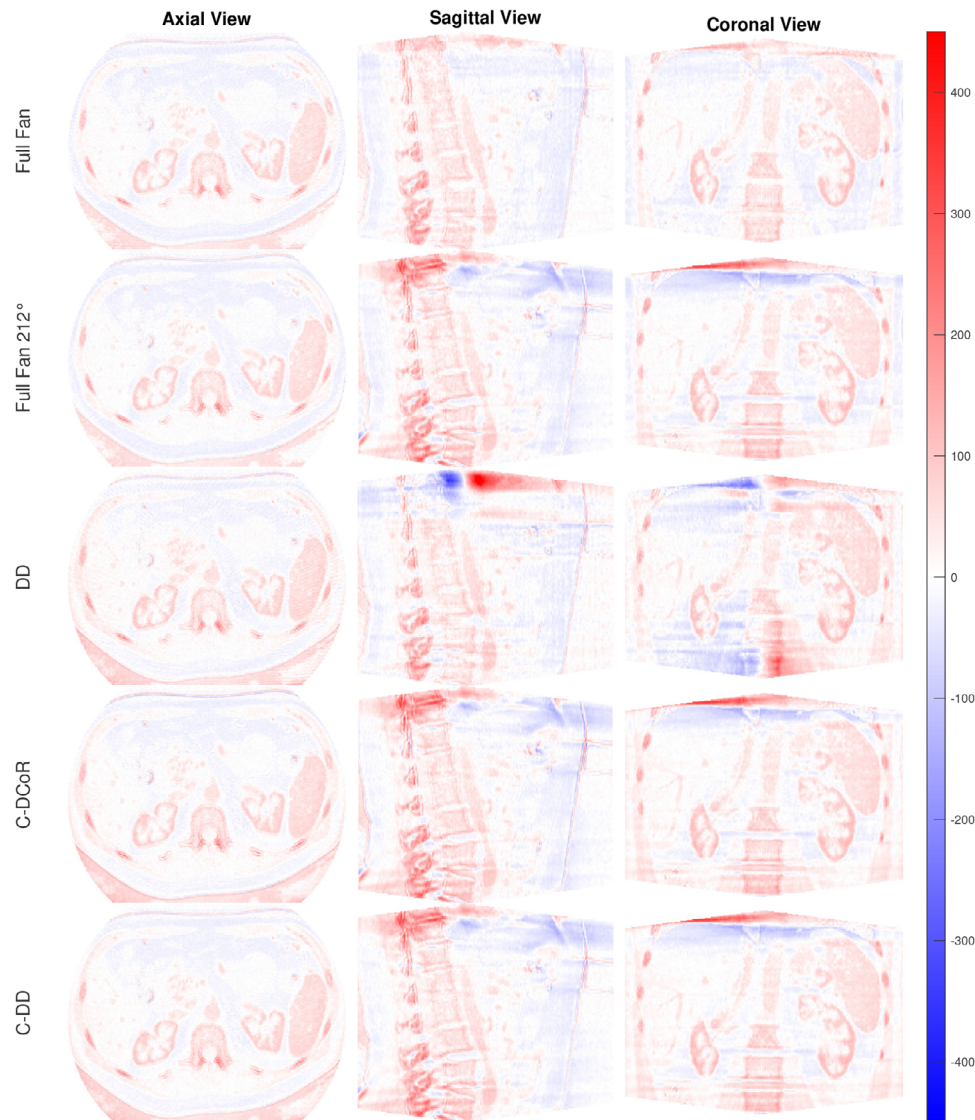


FIGURE 11 Primary-only difference maps for views in Figure 9. The window/level is 900/0 HU.

planning CT into CBCT projections for an estimation of I_p from the projections, requiring the CT to be scaled to CBCT attenuation and for the generated Digitally Reconstructed Radiography (DRR) to be converted into the intensity of the acquired projections. Each DRR derived is then subtracted from the corresponding CBCT projection to obtain the scatter contribution. The latter is smoothed and subtracted from the projection to eliminate only the low-frequency components, that is, the actual scatter, while preserving high frequency components of the primary part I_p . Note that Niu et al. and Park et al.^{22,23} both reference the capability of this method to correct for beam hardening, which would interfere with Joseph and Spital method. Therefore, we did not apply the bone-specific beam-hardening correction to this dataset, and only used the polynomial approach from Equation (10). Each projection dataset was recon-

structed with RTK²⁵ and having applied Equation (10) in the projection domain, $f(x)$ values obtained from Equation (4) are normalized so that $\mu_{water} = 1$ and scaled to HU by applying:

$$CT\# = f(x) * 1000 - 1000 \quad (12)$$

and the FOV was masked out in the resulting CBCT images.

2.5 | Evaluation

Images were evaluated qualitatively by plotting residual differences on central slices. Reconstruction precision and accuracy were reported in terms of global mean absolute error (MAE) and tissue-specific mean error

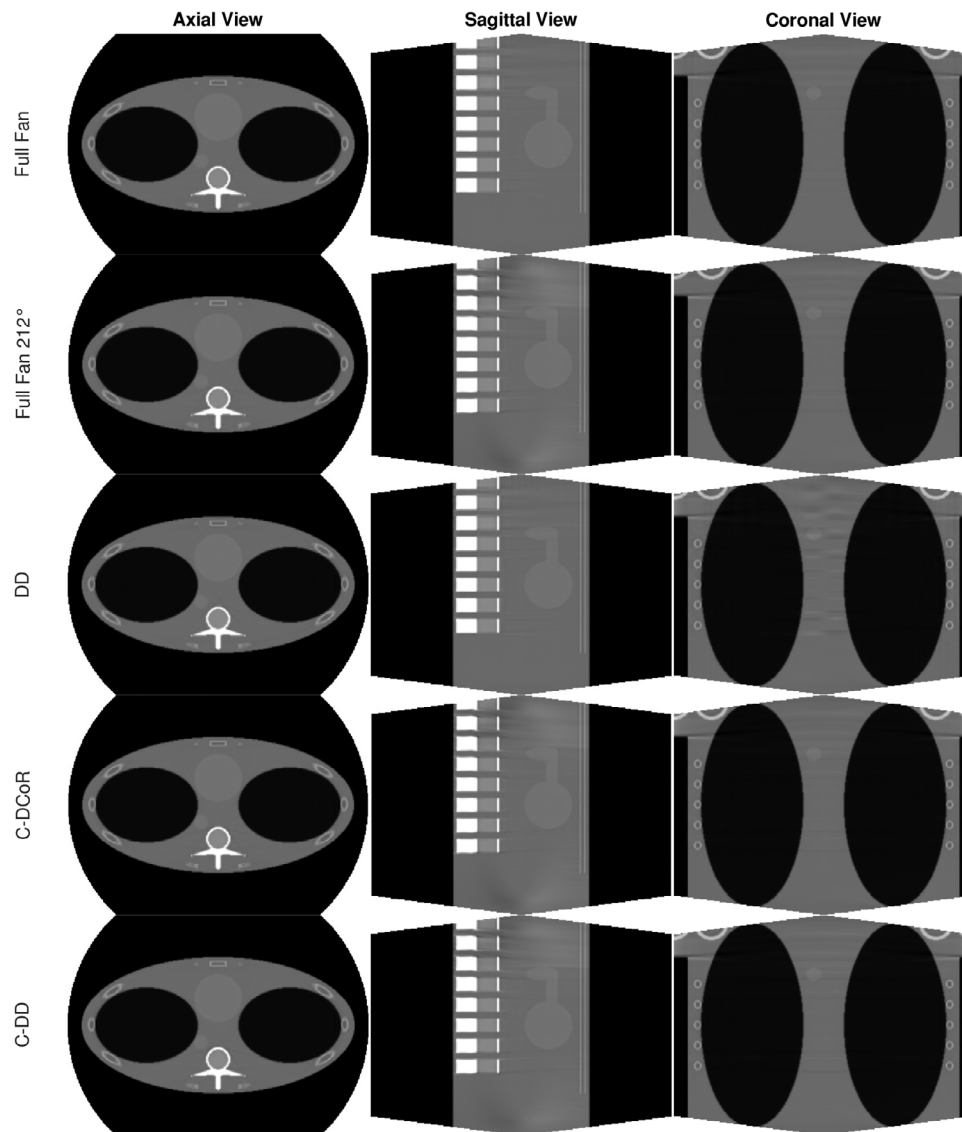


FIGURE 12 Primary-plus-scatter results. The window/level is 1200/0 HU.

(ME) against the original CT image. External air and the carbon couch were excluded from the metrics calculations. For all images, we used a binary mask to select bone values above 920 HU. In the case of the patient data, four additional ROIs of $10\text{ mm} \times 10\text{ mm} \times 10\text{ mm}$ have been extracted in correspondence of fat, muscle, liver, and bone marrow tissues (see Figure 7).

3 | RESULTS

3.1 | Simulations without scatter

Figures 8 and 9 show CBCT images reconstructed from primary projections g_P while Figures 10 and 11 their difference with the ground truth images. The effect of data incompleteness is visible in the sagittal and coronal difference maps with streaks tangential to anatomical

structures whose intensity increases with the distance to the central slice. Notably, these artifacts are especially visible in the coronal view of the 360° DD scan. In the case of the Forbild thorax, the top and bottom parts of the sagittal slices for complementary and FF212° images show an artifact unique to these scans and correlated to the elliptical air volumes representing the lungs in the phantom. This is supported by both the shape of such an artifact and its absence in the patient case (Figures 9 and 11) which presents smaller air gaps. The artifact could stem from the combination of incomplete CBCT data¹⁴ and short scan acquisitions. Patient data in Figures 9 and 11 show inconsistencies at the boundaries between soft tissues and lungs in every scan except the complete FF, with separate patterns on the coronal views of the 360° DD scan and the complementary ones, also replicated in corresponding FF212°. The MAE trend is consistent between complementary

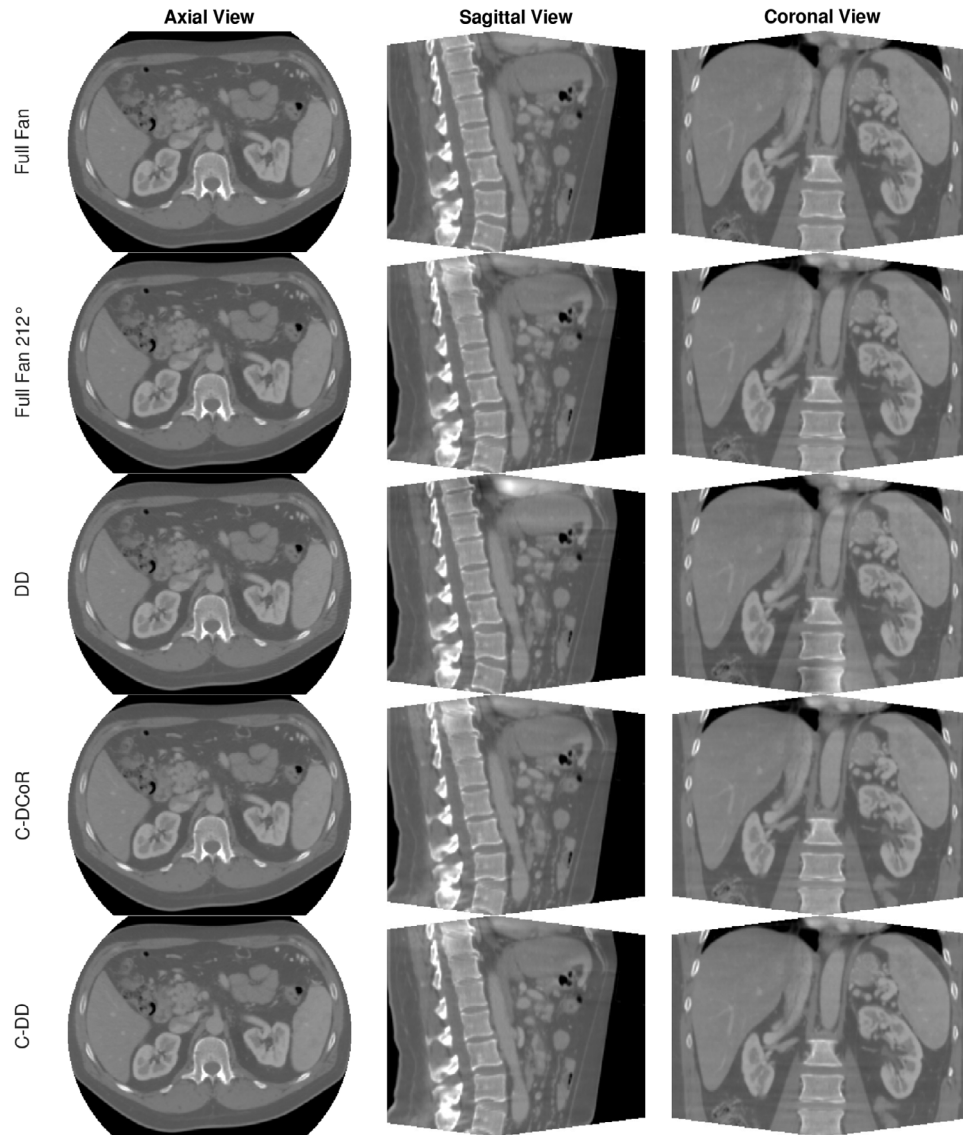


FIGURE 13 Primary-plus-scatter results. The window/level is 1200/0 HU.

and complete datasets (Table 2), where the FF scan is overall the most consistent. The fat and muscle ME in the patient data show similar behavior, except for the DD scans. The latter is influenced by the position of the muscle ROI and the artifact previously described (refer to Figure 7 for ROI positions). The bone ME deviations are limited thanks to the beam hardening correction for bones. Medium-density tissues (liver and bone marrow) have similar deviations across geometries.

3.2 | Primary plus scatter images

CBCT images reconstructed (Figures 12 and 13) from projections with scatter g_{MC} display errors due to data incompleteness plus a slight blurring, as shown in the axial and sagittal views of the complementary and FF212° scans. Residual beam hardening effects are

decreased overall. Artifacts in the sagittal and coronal views (Figures 13 and 14) of the patient data are still prominent and similar to the pattern described in Section 3.1. Notably, interstitial soft tissues near the spine now have lower values w.r.t. the ground truth for all scanning strategies. This is probably due to the scatter correction applied. Global MAE trend in the tabulated data (Table 3) highlights FF as the best among the analyzed strategies, with DD following. The MAE increase of the complementary strategies remains under 16 HU over the FF in the worst case. Comparable MAE (under 11 HU difference) is found between complementary and FF212° scans. Notably, the global MAE for the Forbild phantom is improved w.r.t. to the scatter-less simulations, while it is roughly the same in the patient data case. This is probably due to the effect of blurring over a complex patient anatomy w.r.t. to the phantom uniform inserts. FF achieves better ME results. In the case of fat, a slight

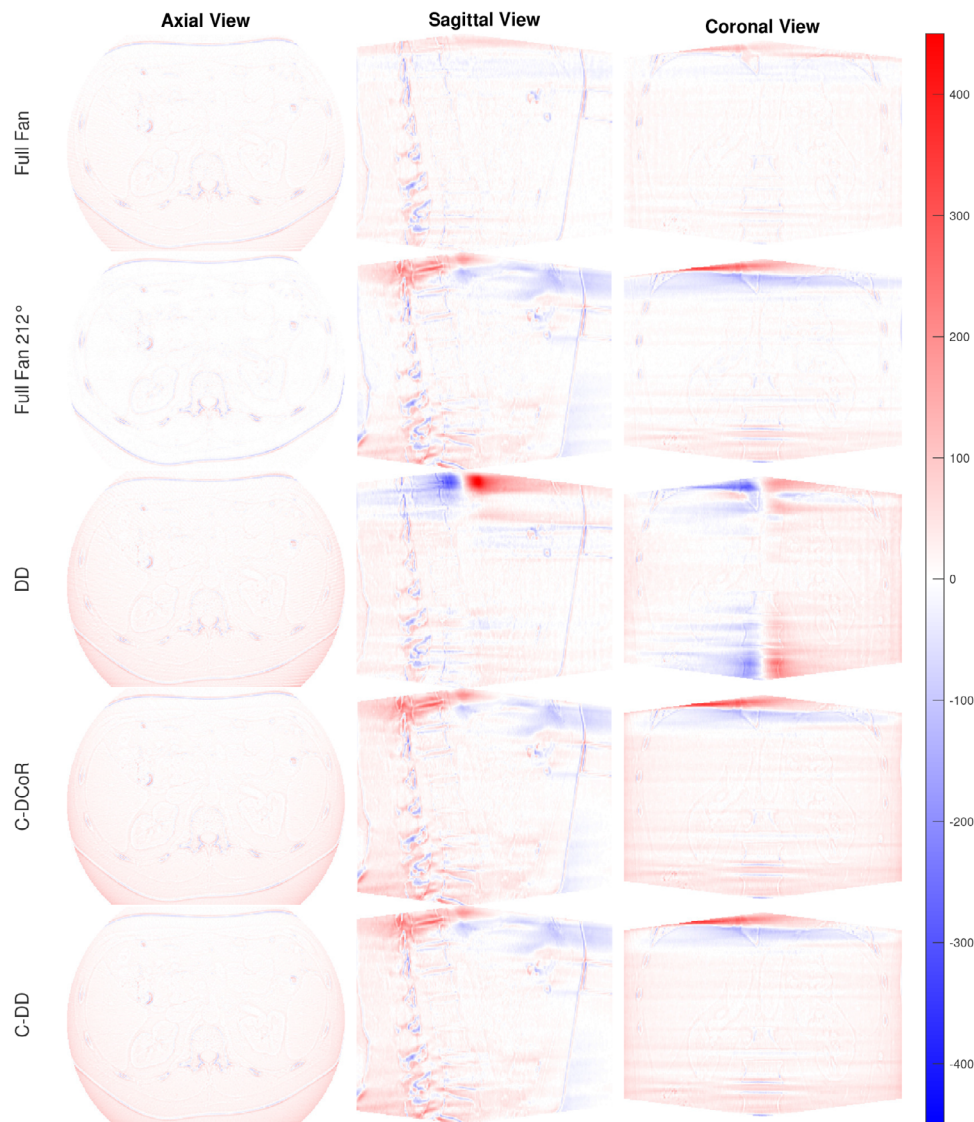


FIGURE 14 Primary-plus-scatter difference maps against CT ground truth for views in Figure 13. Axial view highlights how scatter has been completely removed and residuals about the organs have been lowered w.r.t. 11 The window/level is 900/0 HU. CT, computed tomography.

FOV truncation might negatively influence other scanning geometries. Notably, muscle ME in the DD scan is significantly higher (~ 100 HU), as was the case for primary-only images (Section 3.1).

4 | DISCUSSION

An axial CBCT FOV extension strategy for DD using a couple of short scans has been proposed. Such a method can be used when the detector is tilted, laterally displaced, or a mix of these conditions. Our approach is compatible with on-board imagers mounted onto gantry units with a reduced angular range, provided that it is possible to either offset the detector and collimate the beam onto it or introduce a constant offset to the source-detector bundle during rotation. Previous works have provided sinogram completion strategies to enable the

use of repurposed C-arm instrumentation.⁹ With the growing need for in-room imaging instrumentation, this class of methods will increase the availability of tailored CBCT scanners for diverse applications. Already, the interest for FOV extension in *less than* 360° scanning range has surfaced on a mobile O-arm CBCT scanner.¹³ For IGRT, a large FOV is required for reliable in-room dose map recalculation, which would not be possible with a truncated CBCT. Complementary scanning may be easily implemented as an optional acquisition strategy in various in-room IGRT CBCT scanners, for example, at the CNAO, as it does not require additional hardware or a complete source revolution.

We analyzed potential downsides to image quality with Monte Carlo simulations on two different phantoms. In primary-only images, some artifacts show patterns that are influenced by the short scan approach and

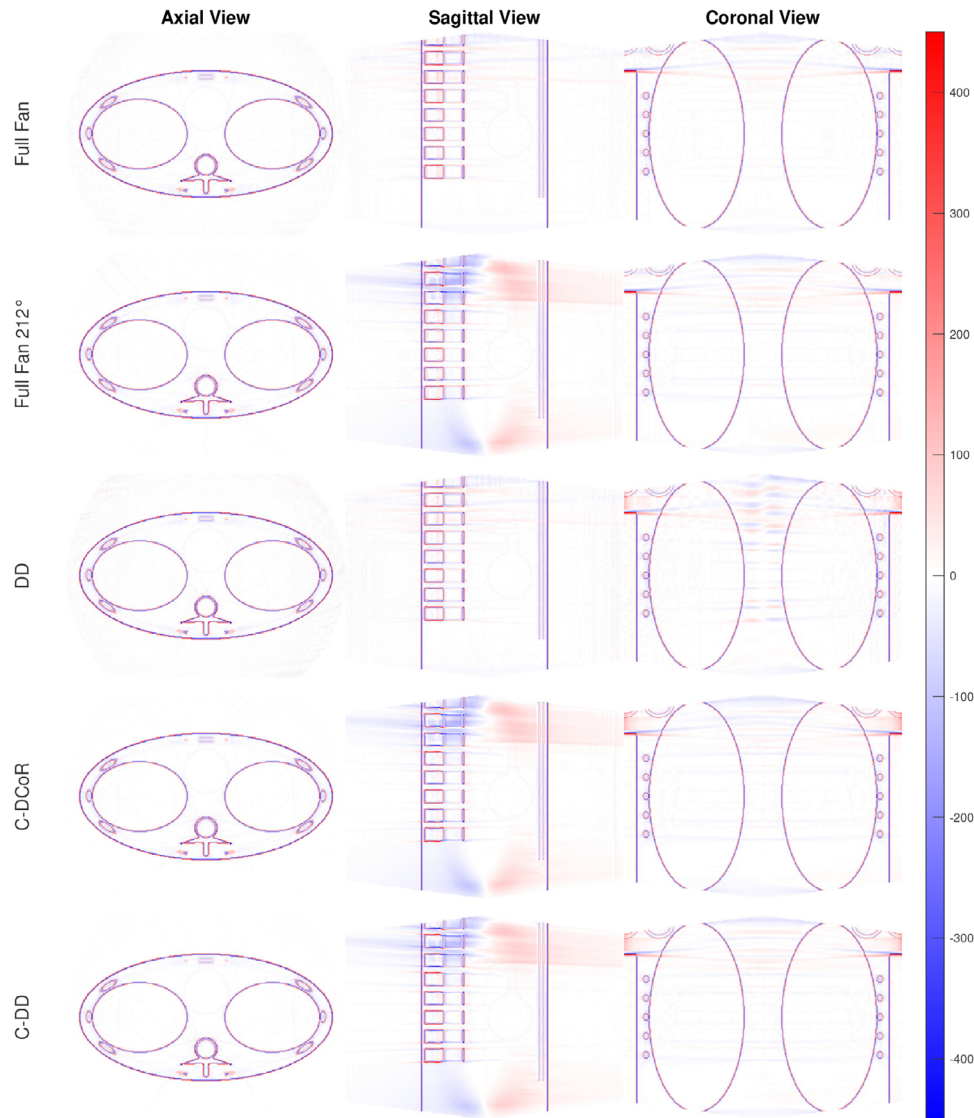


FIGURE 15 Primary-plus-scatter difference maps against CT ground truth for views in Figure 12. Axial view shows how diffused error about the lung tissue, visible in Figure 10, has been removed by the prior CT scatter correction method. The window/level is 900/0 HU. CT, computed tomography.

not tied to the interdependence of the complementary scans, as shown by comparing corresponding data from Subsections 3.1 and 3.2 against FF complete and 220° short scans. Globally, complementary approaches (C-DCoR and C-DD) have lower performance (up to 12 HU higher MAE in the worst case) against complete DD and the untruncated FF complete scan (up to 20 HU higher MAE). We also computed the ME on various tissues finding the complete FF scan to be the best overall, with little evidence supporting DD superiority over C-DCoR and C-DD. In all configurations, there are missing data for exact cone-beam reconstruction except in the source trajectory plane according to Tuy's condition¹⁴ which explains the residual artifacts in Figures 8–15. The level of incompleteness depends on the scan geometry and its impact on the CBCT image quality will also depend on the scanned object.

The prior CT projection-domain scatter correction method on the scattered simulations replicates what a realistic scanner would achieve by accounting for both beam hardening and scatter correction. Globally, complementary approaches (C-DCoR and C-DD) have a slightly lower performance (up to 9 HU higher MAE in the worst case) against complete scan counterpart (DD) and the untruncated FF complete scan (up to 10 HU higher MAE). Finally, the ME analysis on these images resembled the one on the primary images. We recognize that the chosen scatter correction method using prior information heavily relies on the absence of anatomical variations between CT and CBCT scans, possibly introducing an error-prone deformable image registration step. However, given the results in controlled simulations, we argue that other scatter and beam hardening correction methods currently applied to non-complementary

displaced detector scans should perform equivalently on C-DD or C-DCoR scans in a real-world scenario.

5 | CONCLUSION

We have introduced a general formulation for complementary short scans in CBCT imaging. The method can be implemented in any partial gantry or collision-prone on-board imager. A CBCT scan with sufficient FOV enables dosimetric evaluations in the pre-delivery stage of the radiotherapy workflow. Accuracy is mandatory for using such a CBCT image and the image quality of the proposed methods was similar to the short scan acquisition without lateral truncation. Therefore, this method is a valid alternative to state-of-the-art solutions for CBCT FOV extension.

ACKNOWLEDGMENTS

This work was supported by CNAO Foundation (Pavia, Italy) in the project framework entitled “Image guidance-Lateral Room” (reference number BAA9CONV01, 12/03/2019). This work was performed within the framework of the SIRIC LYriCAN+ Grant INCa-DGOS-INSERM-ITMO cancer_18003 and the LABEX PRIMES (ANR-11-LABX-0063) of Université de Lyon, within the program “Investissements d’Avenir” (ANR-11-IDEX-0007) operated by the ANR.

CONFLICT OF INTEREST STATEMENT

The authors have no relevant conflicts of interest to disclose.

DATA AVAILABILITY STATEMENT

The data that support the findings of this study are available on request from the corresponding author. The data are not publicly available due to privacy or ethical restrictions.

REFERENCES

- Landry G, Hua CH. Current state and future applications of radiological image guidance for particle therapy. *Med Phys*. 2018;45:e1086-e1095.
- Fattori G, Riboldi M, Pella A, et al. Image guided particle therapy in CNAO room 2: implementation and clinical validation. *Phys Med*. 2015;31:9-15.
- Deutschmann HSA. MOBILE IMAGING RING SYSTEM Patent:20200121267, 2020.
- Pidikiti R, Patel BC, Maynard MR, et al. Commissioning of the world's first compact pencil-beam scanning proton therapy system. *J Appl Clin Med Phys*. 2018;19:94-105.
- Wang G. X-ray micro-CT with a displaced detector array. *Med Phys*. 2002;29:1634-1636.
- Cho PS, Rudd AD, Johnson RH. Cone-beam CT from width-truncated projections. *Comput Med Imaging Graph*. 1996;20:49-57.
- Penssel C, Kalender WA, Kachelrieß M. ROI-Driven CT Trajectories. In *2006 IEEE Nuclear Science Symposium Conference Record*. 2006;4:1969-1972.
- Parker DL. Optimal short scan convolution reconstruction for fan beam CT. *Med Phys*. 1982;9:254-257.
- Ritschl L, Kuntz J, Fleischmann C, Kachelrieß M. The rotate-plus-shift C-arm trajectory. part I. complete data with less than 180° rotation. *Med Phys*. 2016;43:2295-2302.
- Belotti G, Rit S, Baroni G. Extension of the cone-beam CT field-of-view using two short scans with displaced centers of rotation. In *7th International Conference on Image Formation in X-Ray Computed Tomography At: Baltimore, 2022*.
- Gullberg GT, Crawford CR, Tsui BM. Reconstruction algorithm for fan beam with a displaced center-of-rotation. *IEEE Trans Med Imaging*. 1986;5:23-29.
- Albertini F, Matter M, Nenoff L, Zhang Y, Lomax A. Online daily adaptive proton therapy. *Br J Radiol*. 2020;93:20190594.
- Karius A, Szkitsak J, Strnad V, Fietkau R, Bert C. Cone-beam CT imaging with laterally enlarged field of view based on independently movable source and detector. *Med Phys*. 2023;50(8):5135-5149.
- Tuy HK. An inversion formula for cone-beam reconstruction. *SIAM J Appl Math*. 1983;43:546-552.
- Rit S, Clackdoyle R, Keuschnigg P, Steininger P. Filtered-backprojection reconstruction for a cone-beam computed tomography scanner with independent source and detector rotations. *Med Phys*. 2016;43:2344-2352.
- Feldkamp LA, Davis LC, Kress JW. Practical cone-beam algorithm. *J Opt Soc Am A*. 1984;1:612-619.
- Poludniowski G, Evans P, Hansen V, Webb S. An efficient Monte Carlo-based algorithm for scatter correction in keV cone-beam CT. *Phys Med Biol*. 2009;54:3847.
- Hong J, et al., CT and cone-beam CT of ablative radiation therapy for pancreatic cancer with expert organ-at-risk contours. *Sci Data*. 2022;9:637.
- Jan S, et al. GATE: a simulation toolkit for PET and SPECT. *Phys Med Biol*. 2004;49:4543.
- Poludniowski G, Omar A, Bujila R, Andreo P. SpekPy v2. 0—a software toolkit for modeling x-ray tube spectra. *Med Phys*. 2021;48:3630-3637.
- Joseph PM, Spital RD. A method for correcting bone induced artifacts in computed tomography scanners. *J Comput Assist Tomogr*. 1978;2:100-108.
- Niu T, Sun M, Star-Lack J, Gao H, Fan Q, Zhu L. Shading correction for on-board cone-beam CT in radiation therapy using planning MDCT images. *Med Phys*. 2010;37:5395-5406.
- Park Y-K, Sharp GC, Phillips J, Winey BA. Proton dose calculation on scatter-corrected CBCT image: feasibility study for adaptive proton therapy. *Med Phys*. 2015;42:4449-4459.
- Zöllner C, Rit S, Kurz C, et al. Decomposing a prior-CT-based cone-beam CT projection correction algorithm into scatter and beam hardening components. *Phys Imaging Radiat*. 2017;3:49-52.
- Rit S, Oliva MV, Brousmiche S, et al. The Reconstruction Toolkit (RTK), an open-source cone-beam CT reconstruction toolkit based on the Insight Toolkit (ITK). In *Journal of Physics: Conference Series*, vol. 489. IOP Publishing, 2014: 012079.

How to cite this article: Belotti G, Fattori G, Baroni G, Rit S. Extension of the cone-beam CT field-of-view using two complementary short scans. *Med Phys*. 2024;51:3391–3404. <https://doi.org/10.1002/mp.16869>